sciendo Powder Metallurgy Progress, Vol.20 (2020), No.2, p.081-093
http://dx.doi.org/10.2478/pmp-2020-0008

SINTER HARDENING OF Cr-Mo PRE-ALLOYED STEELS AS A FUNCTION OF THE CARBON CONTENT

Georg Kalss, Christian Gierl-Mayer, Herbert Danninger, Gerold Stetina

Abstract

Sinter hardening is a technique that is frequently employed in powder metallurgy parts production since it is an economical, clean, and environmentally friendly procedure. Since the cooling rates are however significantly lower than e.g. in water or oil quenching, alloy systems have to be used that ensure martensite formation already at moderate cooling rates. In the present study, quenching dilatometry was used to investigate the hardenability of two types of Cr pre-alloyed steels, Fe-3Cr-0.5Mo and Fe-1.5Cr-0.2Mo, the carbon content being varied, and sinter hardening diagrams were plotted. It showed that this parameter has a pronounced influence on the hardenability of the 3 % Cr alloy; in particular in the range 0.3…0.4 % combined C. For the lower alloyed system, in contrast, even 0.52 % combined C was insufficient to ensure martensite formation at the cooling rates typical for industrial sinter hardening. Finally, impact test specimens were prepared by sinter hardening at cooling rates typical for industry, and hardness, as well as impact energy, were determined.

Keywords: sintered steels, sinter hardening, Cr pre-alloyed, martensite, dilatometry.

INTRODUCTION

One of the main reasons for the ubiquitous use of steels is the chance to modify their properties in a wide range by heat treatments [1-3]. Compared to other metals, the ferrite-austenite transformation is the basis for many more variants of heat treatment, in particular the quench-and-temper treatment that has been used for millennia to increase the strength and hardness of steel products. This holds for wrought steels but also for powder metallurgy steels which may differ from wrought steels in composition and microstructure but for which the same fundamentals hold.

With the trend to higher performance combined with lower weight in many areas of technology, in particular in the automotive sector, improved mechanical properties are required also for sintered steels used in powder metallurgy precision parts for highly loaded applications e.g. in automotive engines and transmissions. In this case, advanced alloying concepts are studied, considering the many more alloying variants PM has to offer compared to ingot metallurgy but also the trend to more cost-effective and ecological alloy elements than the usual Cu and Ni in classical PM steels. Here, primarily Cr and Mn are options, to some extent also Si, and prealloying, admixing, diffusion bonding, and master alloys are all viable to produce low alloy steels through the press-and-sinter route.

Georg Kalss, Christian Gierl-Mayer, Herbert Danninger: Technische Universität Wien, Institut für Chemische Technologien und Analytik, Vienna, Austria
Gerold Stetina: Miba Sinter Austria GmbH, Vorchdorf, Austria
Georg Kalss, now: Bühler Group, Leobendorf, Austria

As stated above, heat treatment is a further and widely used route to improve the mechanical properties of sintered steels. This is possible by numerous techniques: the usual quench-and-temper treatment can be applied, this however requires additional manufacturing steps and, since the PM parts contain predominantly open porosity, necessitates careful and extensive cleaning operations to remove the quenching fluid – typically oil – from the pores which is also an ecological penalty. Induction hardening is a standard procedure with high productivity but is restricted to parts such as sprockets with circular symmetry. An elegant and cost-effective method that can be applied to virtually all particle shapes is sinter hardening, i.e. quenching the parts with cold gas – typically nitrogen – immediately after they leave the high-temperature zone of the sintering furnace [4-9]. Sinter hardening furnaces have been available for many years, and this technique has entered large-scale production because of the economical combination of sintering and heat treatment [10]. There is a drawback insofar as sizing is hardly possible with these very hard materials; this is an aspect that has to be considered.

A further limitation is the fairly low cooling rate attainable through gas quenching. In an empty furnace, cooling rates up to 8 K/s are possible but in a fully loaded furnace rates of 2-3 K/s are more realistic. Furthermore, as shown by Bocchini et al [11], the ratio surface/volume also plays a major role since the factor that determines the cooling rate is the heat transfer specimen-atmosphere. Heat conducting within the part itself is usually sufficiently fast to ensure fairly homogeneous cooling – and thus transformation – within the body; here the fact is also beneficial that most PM parts are complex-shaped and thus have a high surface-to-volume ratio and typically low wall thickness.

To compensate for the slow cooling compared e.g. to oil quenching, the alloying system has to be adapted accordingly, with higher alloy element contents being required. Special PM steel grades have been developed for sinter hardening, e.g. based on pre-alloyed Fe-Mo powder with diffusion bonded Cu or Cu+Ni [5, 12]. These alloy elements have been popular in PM because of their low oxygen affinity. Therefore, any oxides present in the compacts can be easily reduced during sintering, and also the risk of oxygen pickup from the sintering atmosphere is marginal. However, these elements are expensive, and Ni is classified as carcinogenic; consequently, elements such as Cr are increasingly regarded as attractive [13], and Cr and Cr-Mo pre-alloyed powders are now commercially available at an acceptable cost. These powders result in tighter requirements regarding the chemistry of sintering, but this is manageable today, and it has been shown that this class of materials is also well suited for sinter hardening [7], at least if martensite is the desired microstructure.

In the present work, sinter hardening of steels prepared from such pre-alloyed powder grades has been investigated with the main focus on the role of carbon in combination with high-temperature sintering [14-16]. Carbon control is essential for sintered steels, being trickier than with wrought steels, and particular with sintered steels alloyed with elements of high oxygen affinity such as Cr, carbon loss during sintering is a crucial topic. This holds true in particular for high-temperature sintering when deoxidation is more complete but at the price of higher carbon loss [17]. Therefore, the role of the combined C content on the sinter hardening response of PM steels is of high practical relevance.

EXPERIMENTAL PROCEDURE

As starting materials, the pre-alloyed steel grades Astaloy CrM (Fe-3%C-0.5%Mo) and Astaloy CrL (Fe-1.5%Cr-0.2%Mo) were used, both from Höganäs AB, Sweden. Natural graphite UF4 (Kropfmühl) was admixed as a carbon source, and Licowax C

Micropowder PM (Clariant) was added as a lubricant. The powders were compacted at 800 MPa to test bars 100 x 10 x 9 mm^3, the resulting green densities (measured through mass and dimensions) being approx. 7.02 $g.cm^{-3}$ for CrM and 7.07 $g.cm^{-3}$ for CrL. The green compacts were sintered in a push-type furnace with SiC heating elements and gas-tight superalloy muffle (Kanthal APM) for 40 min isothermal at 1250°C (Ast CrM) or 1280°C (Ast CrL), the latter temperature being slightly higher to compensate for the slightly lower sintering activity of CrL as a consequence of its lower Cr content. The sintering atmosphere was high purity N_2 (99.999 %).

At the end of the furnace, a gas quench unit was fixed that allowed defined sinter hardening by nitrogen quenching, the cooling conditions being adjusted by setting the nitrogen flow accordingly, a range of 8…78 m^3/hr being used. The cooling process was recorded by a thermocouple fixed in the bore of a dummy specimen that was placed in the sintering boat together with the specimens to be sinter hardened. Since the gas flow was kept constant during each cooling cycle, exponential cooling graphs were obtained (in contrast to classical CCT diagrams, but similar to the actual conditions in the sinter hardening furnace), and the hardenability was plotted in "sinter hardening diagrams" in which the time axis was set linear (see e.g. [6]). The sintered density was measured through water displacement (after impregnation of the specimens with water stop spray), and apparent hardness HV30 and unnotched impact energy were measured.

From the sinter hardened specimens, small bars of 12 x 4 x 4 mm3 were cut, and thermocouples Type S were welded to the bars. The specimens were then inserted into a quenching dilatometer Bähr type 805, heated at 25 K/s to 1100°C, held there for 5 min in a vacuum, and then quenched with Ar 99.999 %, the desired cooling profile being attained by adjusting the Ar flow. Afterward, the specimens were characterized metallographically.

To ease the comparison of the (exponential) cooling cycles, a cooling rate linearized between 1100 and 100°C is given in the following. The austenitizing temperature of 1100°C, which is extraordinarily high for standard CCT diagrams, was used to approximate the conditions for sinter hardening in which case gas quenching is typically done from 1120°C, in part even from 1250°C. The otherwise critical austenite grain coarsening, which would occur in wrought steels at these high temperatures, is not a problem with sintered steels since the pores stabilize the grain structure [18].

RESULTS

Sinter hardening diagram for Astaloy CrM

For this test run, specimens were prepared to contain 0.4 %, 0.5 %, and 0.6 % C admixed; after sintering the combined carbon content was measured by LECO analysis to be 0.30, 0.39, and 0.49 % C, respectively. Higher C contents were avoided according to the results shown in [19]. Quenching tests were done from 1100°C at different conditions, the linearized cooling rates being varied from 1 to 8 K/s, in part up to 16 K/s.

In Fig. 1, typical dilatometric graphs and the resulting microstructures are shown. As can be seen, at 1 K/s bainitic transformation occurs, while at 2.5 K/s a mixed bainitic-martensitic microstructure is generated, and at 4 K/s fully martensitic transformation is recorded. This however means that for industrial practice, at this carbon content the material is not sufficiently reliable for sinter hardening since no fully martensitic microstructure can be expected.

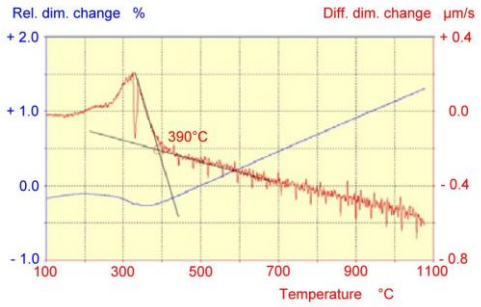

a) dilatometric graph

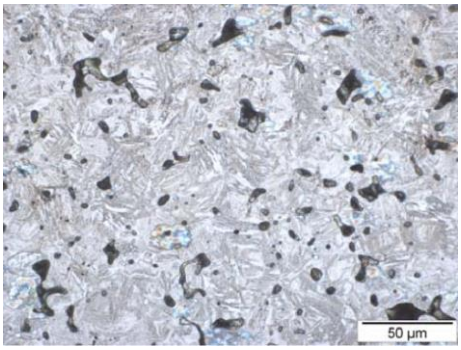

b) section, Nital etched

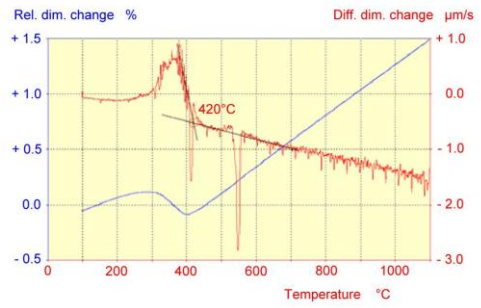

c) dilatometric graph

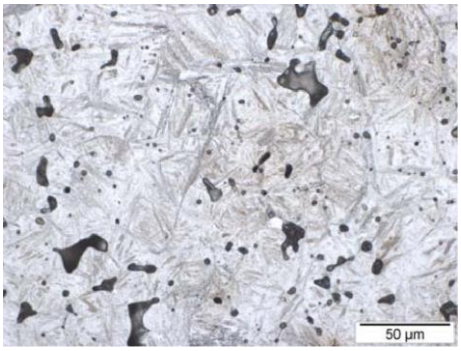

d) section, Nital etched

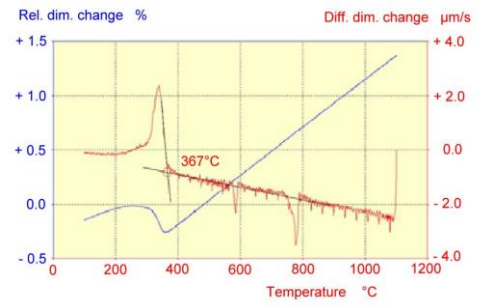

e) dilatometric graph

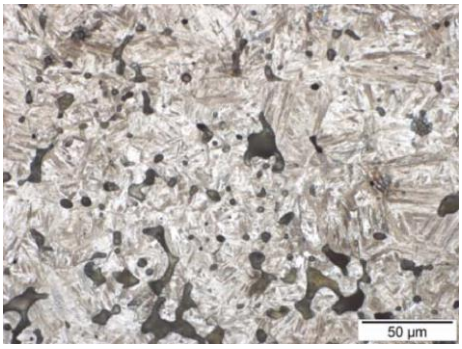

f) section, Nital etched

Fig. 1. Quenching dilatograms and microstructures of Astaloy CrM-0.30%C(combined), differently cooled: a,b) linearized cooling rate 1 K/s; c,d) linearized cooling rate 2.5 K/s; e,f) linearized cooling rate 4 K/s.

When the carbon content is increased to 0.39 % combined, significantly different behavior is observed (Fig. 2). At 1 K/s a mixed bainitic-martensitic transformation is recorded, but already at 1.5 K/s a virtually martensitic microstructure is generated, and the same holds for 2 K/s. This means that this material is already suited for application in industrial sinter hardening furnaces, at least if the precise adjustment of the carbon content is granted.

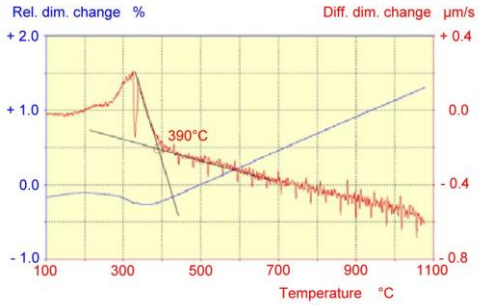

a) dilatometric graph

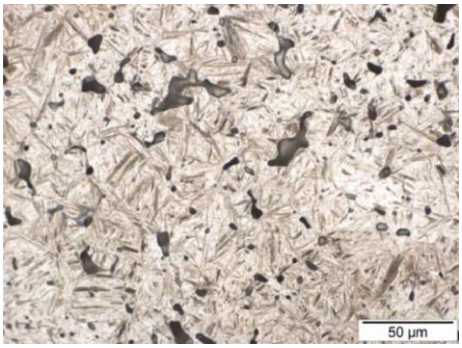

b) section, Nital etched

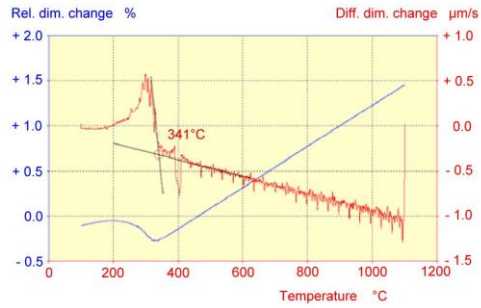

c) dilatometric graph

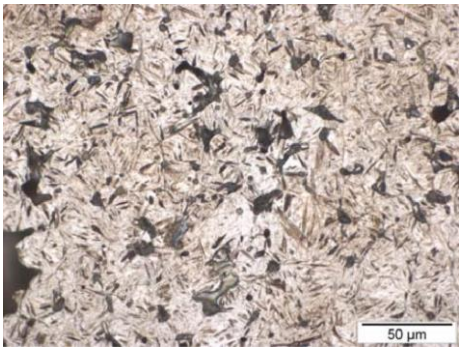

d) section, Nital etched

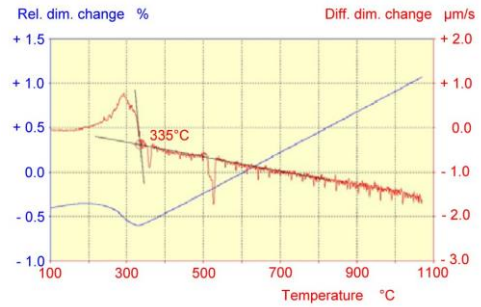

e) dilatometric graph

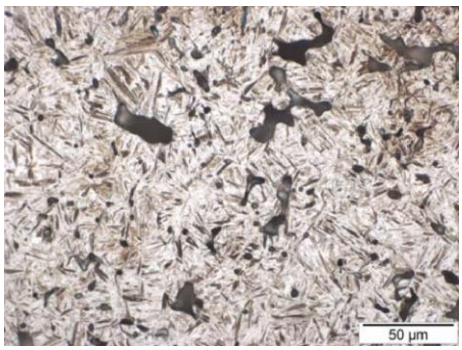

f) section, Nital etched

Fig. 2. Quenching dilatograms and microstructures of Astaloy CrM-0.39%C(combined), differently cooled: a,b) linearized cooling rate 1 K/s; c,d) linearized cooling rate 1.5 K/s; e,f) linearized cooling rate 2 K/s.

If the carbon content is further increased, to 0.49 % combined, the hardenability is improved once more (Fig. 3): here, even at a cooling rate of 0.5 K/s some martensite is formed alongside bainite, and at 1 K/s fully martensitic microstructure is generated. This indicates that the material is very robust in sinter hardening, even larger and thick-walled specimens transforming fully martensitic under industrial cooling conditions.

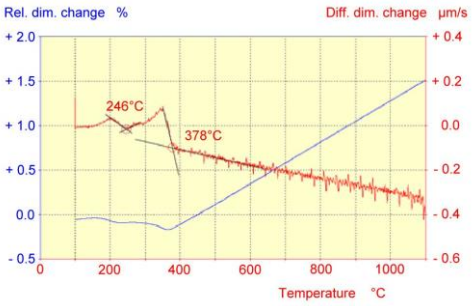

a) dilatometric graph

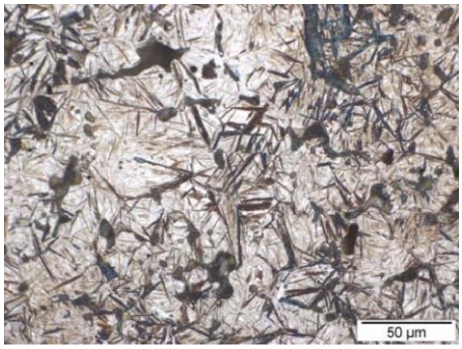

b) section, Nital etched

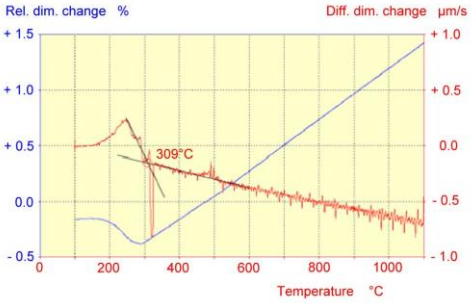

c) dilatometric graph

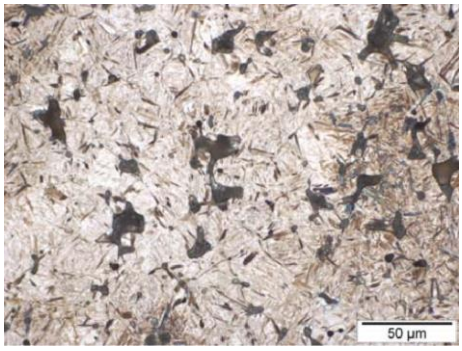

d) section, Nital etched

Fig. 3. Quenching dilatograms and microstructures of Astaloy CrM-0.49%C(combined), differently cooled: a,b) linearized cooling rate 0.5 K/s; c,d) linearized cooling rate 1 K/s.

When a sinter hardening diagram is plotted for the materials, the very pronounced effect of the carbon content is evident. As expected, the Ms temperature drops with higher C levels and the bainite area is shifted significantly to the right: while at 0.30 % C 3 K/s cooling rate is barely sufficient to generate martensite, at 0.49 % C even at 1 K/s fully martensitic structure is attained. This strong dependence of the hardenability on the carbon content underlines the enormous importance of careful carbon control which on one hand means control of the sintering atmosphere – to avoid decarburization –, but on the other hand also precise control of the starting oxygen content of the steel powder. The reason is that, as shown e.g. in [17, 20] in this type of PM steel, carbon is the only effective reducing agent; even if sintering in an H_2-containing atmosphere, the fraction of oxygen removed by the formation of H_2O in the 400°C range is rather insignificant [17], and any change of the starting oxygen content means a change of the combined carbon and thus of the hardenability.

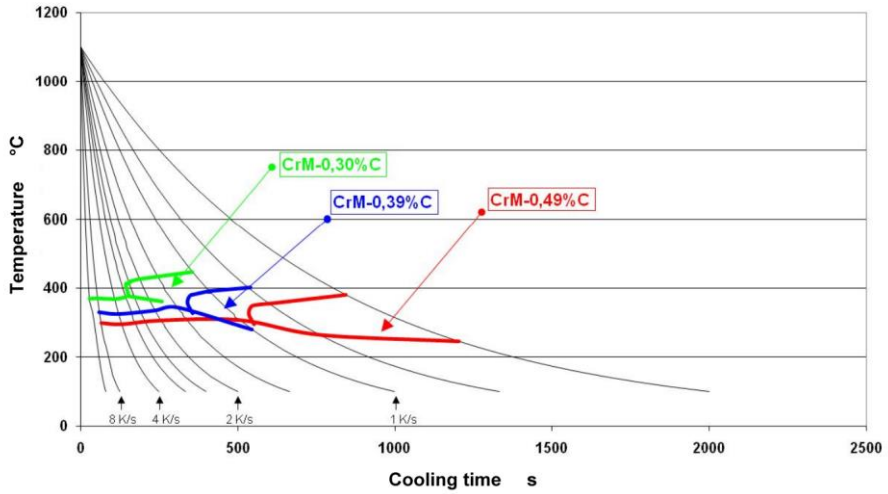

Fig. 4. Sinter hardening diagram of Astaloy CrM-x%C with varying carbon contents. Compacted at 800 MPa, sintered 40 min at 1250°C in N_2.

It can therefore be concluded that a carbon content of 0.4 % C (combined) is sufficient to ensure sinter hardening under industrial conditions. Another fact that should be considered however is the hardness attained through a martensitic transformation; hardness and hardenability are different properties [4]. It is well known (see e.g. [3]) that the hardness of martensite depends on the carbon content. To check the hardness attainable here, the microhardness was measured on specimens cooled with a rate that granted fully martensitic transformation. The results are shown in Tab. 1.

Tab. 1 Microhardness HV0.05 of Astaloy CrM-C with varying C contents, sintered 40 min at 1250°C and quenched to martensitic microstructure.

Carbon content wt. %		**Microhardness HV 0.05**	
C admixed	**C combined**	**Cooling rate 4 K/s**	**Cooling rate 8 K/s**
0.40	0.30	467	472
0.50	0.39	588	592
0.60	0.49	691	690

These data clearly show that even if sintered steel is hardened to fully martensitic microstructure, only moderate matrix hardness is attained at low carbon levels. This means that for attaining high hardness the carbon content has a double effect, on the one hand improving the hardenability – i.e. the probability to obtain martensitic microstructure at a given cooling regime – and on the other hand to establish sufficient hardness of this martensite. There is of course also the question of toughness, which is also related to the hardness; this will be discussed later.

Another parameter of relevance is the Ms temperature. In Tab. 2, the Ms temperatures measured from the cooling curves for 4 and 8 K/s (linearized), respectively, are plotted; as stated above, at these cooling rates fully martensitic microstructure was obtained in all cases. As expected, the Ms temperature drops with higher carbon content

while the differences between the cooling rates are within the experimental scatter. To check if the measured Ms temperatures agree with the models available in the literature, the equations proposed by Steven and Haynes [21] and Andrews [22], respectively, as given in [3] were used, and the calculated values are depicted in Tab. 2.

Tab. 2 Ms temperatures, measured vs. calculated, of Astaloy CrM-C with varying C contents, sintered 40 min at 1250°C and quenched to martensitic microstructure.

Carbon content wt. %		**Ms temperature exper. °C**		**Ms calculated °C**		
C admixed	**C combined**	**Cooling rate 4 K/s**	**Cooling rate 8 K/s**	**Steven and Haynes**	**Andrews linear**	**Andrews product**
0.40	0.30	367	370	357	372	375
0.50	0.39	325	330	314	334	329
0.60	0.49	295	299	267	292	283

The formula given by Steven and Haynes somewhat underestimates the Ms temperature while the equations from Andrews (product) and in particular Andrews (linear) predict the temperature quite reliably within the tolerated scatter. This once more confirms that such data available for wrought steels can be applied to sintered steels as well, at least for those with fairly homogeneous microstructure, as is the case with the pre-alloyed steels investigated here.

When taking the final dimensional changes observed from the dilatometric graphs – as far as can be derived from these graphs - it can be seen that the behavior is close to dimensional stability, the net dimensional change being close to +/-0 in most cases without much dependence on the carbon content or the microstructure. Here, however, more detailed investigations are currently being carried out with a newly acquired quench dilatometer.

Sinter hardening diagram for Astaloy CrL

For Astaloy CrL-C with the same nominal carbon contents, similar experiments were carried out. Here it showed that irrespective of the carbon content the hardenability is much lower than for CrM, which underlines the high relevance of the metallic alloy elements Cr and, to a lesser degree, Mo. In Fig. 5, typical dilatograms are shown, and it is evident that even at fairly high cooling rates bainite predominantly is formed. The respective sinter hardening diagram is shown in Fig. 6.

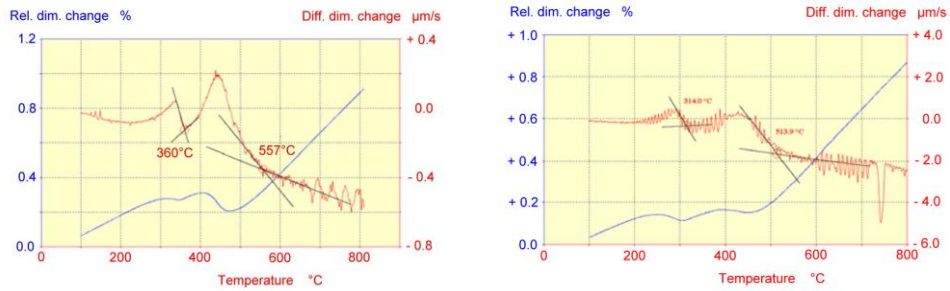

a) 0.32 % C combined, 8 K/s (linearized) b) 0.42 % C combined, 4 K/s (linearized)

Fig. 5. Quenching dilatograms of Astaloy CrL-x%C, compacted at 800 MPa, sintered 40 min at 1280°C in N_2.

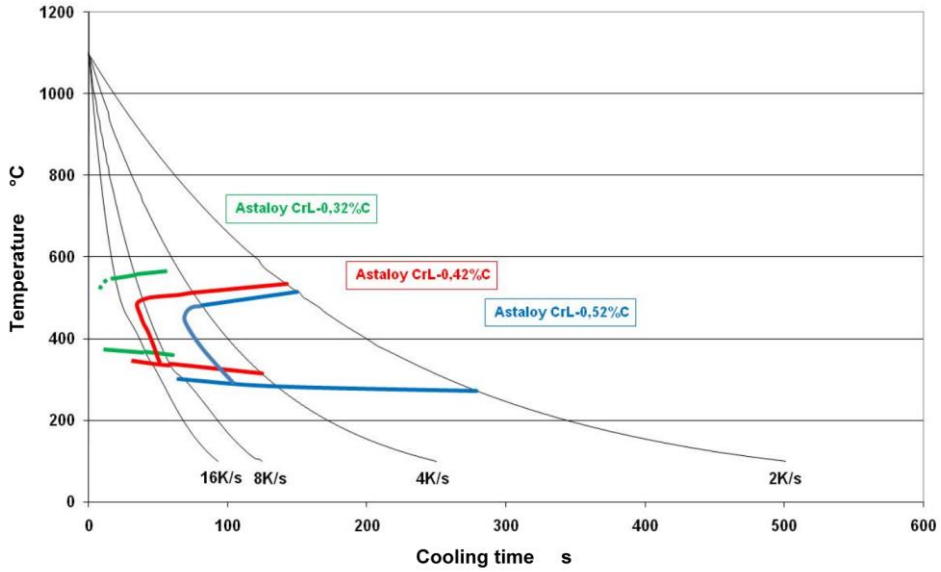

Fig. 6. Sinter hardening diagram of Astaloy CrL-x%C, compacted at 800 MPa, sintered 40 min at 1280°C in N_2.

From this diagram, it stands out clearly that the effect of carbon on the hardenability is markedly less pronounced for Astaloy CrL than for CrM. Even for the highest carbon content of 0.52 % C combined (0.6 % C nominal) cooling rates > 4 K/s are required to obtain martensitic microstructures. For lower C levels, accordingly higher cooling rates are required, > 8 K/s for 0.42 C combined and >16 K/s for 0.32 % C combined. These cooling rates are far higher than what can be attained in industrial practice; i.e. in contrast to Astaloy CrM, CrL by itself is not suited for sinter hardening even at higher carbon contents (too high C levels should be avoided to prevent loss of ductility). If sinter hardening is being aimed at, further alloy elements should be added such

as e.g. Cu [13, 23], but also master alloys containing Mn, Cr, and/or Si are effective [24-26].

Mechanical properties

Typically, the penalty to be paid for high hardness is low ductility, in sintered steels measured best through the impact energy. Therefore, it was to be checked if the positive hardening behavior of the CrM materials was combined with at least acceptable impact resistance.

To assess the properties of sinter hardened specimens prepared from both starting powder grades, impact test bars were prepared and sintered at 1250/1280°C, respectively, with subsequent sinter hardening in the gas quenching unit of the sintering furnace. By adjusting the N_2 flow, 2 cooling rates were attained, 2.2 and 2.7 K/s (linearized) to approximate the upper and lower boundaries of the cooling rate range in industrial furnaces. The properties are shown in Tab. 3.

Tab. 3 Dimensional and mechanical properties of Cr-Mo pre-alloyed sintered steels, compacted at 800 MPa, sintered 40 min in high purity N_2, sinter hardened at 2 different rates, and tempered 40 min at 200°C.

C (admixed) wt. %	C (combined) wt. %	Green density g.cm^{-3}	Cooling rate K/s lin.	Sintered density g.cm^{-3}	Apparent hardness HV30	Impact energy (unnotched) J.cm^{-2}
Astaloy CrM, sintered at 1250°C						
0.40	0.30	7,019	2.2	7.191±0.013	307±9	34.7±2.1
0.40	0.30	7.019	2.7	7.203±0.000	320±9	33.9±3.1
0.50	0.39	7.011	2.2	7.195±0.000	398±2	34.1±2.8
0.50	0.39	7.011	2.7	7.201±0.001	411±5	38.3±1.2
0.60	0.49	7.008	2.2	7.193±0.008	434±9	36.0±3.6
0.60	0.49	7.008	2.7	7.203±0.002	444±9	38.0±2.8
Astaloy CrL, sintered at 1280°C						
0.40	0.32	7,073	2.2	7.258±0.003	194 ± 2	42.5±3.5
0.40	0.32	7.073	2.7	7.256±0.000	186 ± 1	43.6±1.5
0.50	0.42	7.064	2.2	7.249±0.002	204 ± 1	42.4±1.9
0.50	0.42	7.064	2.7	7.250±0.002	207 ± 4	41.7±1.4
0.60	0.52	7.059	2.2	7.252±0.003	216 ± 4	40.2±0.8
0.60	0.52	7.059	2.7	7.253±0.002	229 ± 6	42.4±2.1

As can be seen from the table, in agreement with the previously shown results Astaloy CrM exhibits hardening at both cooling rates while Astaloy CrL remained soft regardless of cooling rate and carbon content, which corroborates the findings from quench dilatometry that this latter material is not suited for industrial sinter hardening, unless further alloy elements are added.

Astaloy CrM, in contrast, exhibits a surprisingly attractive combination of hardness and toughness, and this is improved at higher carbon levels, the impact energy being virtually independent of the combined carbon while the hardness increases with higher C content, as already indicated by the microhardness data (the differences between apparent hardness HV30 and microhardness HV0.05 are mainly a consequence of pore compression in the former test). The attractive property profile of sinter hardened Astaloy CrM is particularly well visible when plotting the impact energy vs. the hardness, as shown

in Fig. 7. Here it is evident that the CrM based materials exhibit only marginally lower impact energy than the much softer CrL types and that for CrM higher C content results in higher hardness and at least the same if not higher impact energy.

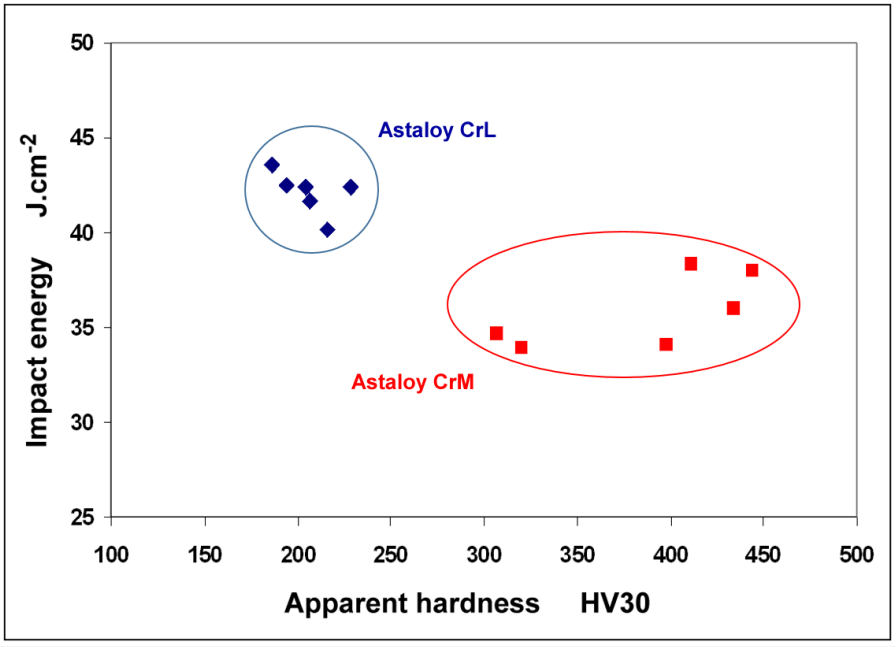

Fig. 7. Impact energy vs. apparent hardness of Astaloy CrM and Astaloy CrL after processing as in Table 2

CONCLUSIONS

Experiments in a quenching dilatometer were performed on sintered steels prepared from Cr-Mo pre-alloyed powders. It showed that for steel grades alloyed with 3%Cr-0.5%Mo, the hardenability strongly depends on the carbon content: while for 0.30 % C combined (0.40 % admixed), a minimum cooling rate of 4 K/s (linearized between 1100 and 100°C) is required to obtain fully martensitic microstructure, at 0.39 % C combined the threshold is at 1.5 K/s, and for 0.49 % C combined a cooling rate as low as 1 K/s is sufficient to percent bainite formation and result in martensite. Sinter hardening diagrams – modified CCT-diagrams – were plotted to show these relationships; for the moderate cooling rates employed for sinter hardening these diagrams with a linear time axis are more significant than classical CCT diagrams.

The lower alloyed system containing 1.5%Cr-0.2%Mo, in contrast, required markedly higher cooling rates; even at carbon levels >0.5 % combined cooling rates >4 K/s are required to ensure martensite formation. Considering that in industrial practice the cooling rates attainable are usually in the range of 2-3 K/s at least in fully loaded furnaces it can be concluded that the higher alloyed grade is well suited for sinter hardening if the carbon content is properly adjusted and carefully controlled while the lower alloyed variant does not sinter harden under industrial conditions unless further alloy elements are added.

Mechanical testing on materials sinter hardened under industry-relevant conditions showed that while the lower alloyed variant exhibited high impact toughness but low hardness, as a consequence of the poor hardenability, the higher alloyed steel had slightly

lower impact energy but much higher hardness, in particular at higher carbon levels, and the impact energy did not decrease with more combined C. This shows that the 3Cr-0.5Mo steel is excellently suited for sinter hardening of highly loaded PM components.

REFERENCES

[1] Ed. Houdremont: Handbuch der Sonderstahlkunde. Springer, Berlin-Göttingen-Heidelberg, 1956.
[2] ASM Handbook Vol.4 „Heat Treating“, ASM, Materials Park OH, 1991.
[3] Krauss, G.: Steels – Structure, Processing, and Performance. ASM Materials Park OH, 2005.
[4] Brian James, W.: What is sinter hardening? Proc. PM2 TEC '98 Las Vegas, MPIF, Princeton NJ, 1998.
[5] Engström, U.. In: Proc. PowderMet 2000 New York, MPIF, Princeton NJ, Part 5, 2000, p. 157.
[6] Semel, FJ.: Cooling rate effects on the metallurgical response of a recently developed sintering hardening grade. Adv. Powder Metall. & Partic. Mater. -2002, MPIF, Princeton NJ, Part 13, 2002, p.102.
[7] Maroli, B., Berg, S., Thorne, P., Engström, U. In: Proc. PM2TEC’03 Las Vegas, MPIF, Princeton NJ, 2003.
[8] Stoyanova, V., Molinari, A.: Powder Metall. Progress, vol. 4, no. 2, 2004, p. 79.
[9] Yu, Y. In: Proc. PMAsia2007, Shanghai, China, 2007.
[10] Ratzi, R., Orth, P.: Metal Powder Rep., vol. 55, no.7/8, 2000, p. 20.
[11] Bocchini, GF., et al.: Influence of density and surface/volume ratio on the cooling speed of sinter-hardening materials, Part two: Microstructure and microhardness distribution inside parallelepipeds. Adv. Powder Metall. & Partic. Mater. – 2002, MPIF, Princeton NJ, Part 13, 2002, p. 60.
[12] Karamchedu, S., Hatami, S., Nyborg, L., Andersson, M.: Powder Metall. Progress, vol. 14, no.2, 2014, p. 93.
[13] Berg, S., Maroli, B.: Properties obtained by chromium-containing material. Adv. Powder Metall. & Partic. Mater. -2002, MPIF, Princeton NJ, Part 8, 2002, p. 1.
[14] Engström, U., Mc.Lelland, J., Maroli, B.: Effect of sinter hardening on the properties of high temperature sintered PM steels. Adv. Powder Metall. & Partic. Mater. – 2002, MPIF, Princeton NJ, Part 13, 2002, p. 1.
[15] Dlapka M. et al: Powder Metall. Progress, vol. 10, no.1, 2010, p. 20.
[16] Dlapka, M., Danninger, H., Gierl, C., Lindqvist, B.: HTM - Journal of Heat Treatment and Materials, vol. 67, no.3, 2012, p. 223.
[17] Danninger, H., Gierl, C.: Sci. Sintering, vol. 40, no.1, 2008, p. 33.
[18] Dlapka, M., Strobl, S., Danninger, H., Gierl, C.: Pract. Metallography, vol. 47, no. 12, 2010, p. 686.
[19] Berg, S. In: Proc. PM2004 Powder Metallurgy World Congress Vienna, EPMA, Shrewsbury UK, Vol.3, 2004, p. 53.
[20] Danninger, H., de Oro Calderon, R., Gierl-Mayer, C.: Powder Metall., vol. 61 no. 3, 2018, p. 241.
[21] Steven, W., Haynes, AG.: J. Iron Steel Inst., vol. 183, 1956, p. 349.
[22] Andrews, KW.: J. Iron Steel Inst., vol. 203, 1965, p. 721.
[23] Chagnon, F., Trudel, Y.: Effect of copper additions on properties of 1.5%Mo sintered steels. Adv. Powder Metall. & Partic. Mater. -2002, MPIF, Princeton NJ, Part 13, 2002, p. 73.
[24] de Oro Calderon, R., Gierl-Mayer, C., Danninger, H.: Powder Metallurgy Review, vol.

5, no.3, 2016, p. 59.
[25] de Oro Calderon, R., Jaliliziyaeian, M., Dunkley, JJ., Gierl-Mayer, C., Danninger H. In: "Proceedings WorldPM2018", The Chinese Society for Metals, Beijing, 2018, p. 1943.
[26] Gierl-Mayer, C., de Oro Calderon, R., Danninger H.: BHM Berg- und Hüttenmännische Monatshefte, vol. 164 no. 9, 2019, p. 372.

Powder Metallurgy Progress, Vol.20 (2020), No.2, p.094-103
http://dx.doi.org/10.2478/pmp-2020-0009

X-RAY PHOTOELECTRON SPECTROSCOPY STUDY OF EUROPIUM NIOBATE THIN FILM PREPARED BY CHEMICAL SOLUTION DEPOSITION

Helena Bruncková, Maria Kaňuchová, Hristo Kolev, Erika Múdra, Alexandra Kovalčiková, Ľubomír Medvecký

Abstract

Transparent europium niobate $EuNbO_4$ (ENO_F) thin film (~100 nm) was prepared by sol-gel/spin-coating process on alumina substrates with $PbZrO_3$ (PZ) interlayer and annealing at 1000°C. The X-ray diffraction (XRD) analyses verified the formation of the monoclinic M-$EuNbO_4$ and tetragonal T-$EuNb_5O_{14}$ phases in ENO precursor and ENO_F film. The surface morphology of powder precursor and microstructure of film were investigated by SEM analyses. Surface chemistry was investigated by X-ray photoelectron spectroscopy (XPS). The XPS demonstrated two valence states of Eu (Eu^{3+}/Eu^{2+}) in powder precursor as nanophosphor for lighting and display technologies. Eu concentration (at. %) decreases from 10 % in the precursor to 2 % in the film considering the substrate contains C, Al, Si, Pb, and Zr elements (40 %) at Nb (6 %) and O (52 %). The single valence state of Eu^{3+} was confirmed in ENO film designed for the application in environmental electrolytic thin-film devices.

Keywords: sol-gel, thin films, EuNbO4, microstructure, Spectroscopy, XPS

INTRODUCTION

Lanthanide niobates ($LnNbO_4$) have been attracting interest due to their excellent and interesting properties in the fields of luminescence, ionic conductivity, photocatalytic activity, magnetic properties, and crystal structures [1]. Ferroelastic $LnNbO_4$ is being researched for diverse applications, according to their individual properties [2]. The investigative fields of $LnNbO_4$ include proton-conducting solid oxide fuel cells, microwave dielectric materials, and shape memory materials [2]. Europium niobate $EuNbO_4$ (ENO) ceramics and film have possessed mixed types of conduction processes, including protonic, ionic, and electronic conduction which is determined by fabrication conditions, and these materials are promising for sensors, solid fuel cell electrolytes, and high-temperature proton conductors [1,3-5]. The excellent material mechanical properties of $EuNbO_4$ imply that ENO is a promising thermal barrier coating [2]. It also possesses excellent photoluminescence properties. ENO is a material with high potential in optoelectronics as a light emitter [5]. Microwave dielectric $EuNbO_4$ ceramics are widely used in GPS antenna technology, dielectric waveguide circuits, radar, and wireless communication devices [6]. For ENO, there are two crystalline forms, the low-temperature M-phase isostructural with a monoclinic form of the fergusonite and the T-phase corresponding to tetragonal scheelite [7,8].

Helena Bruncková, Erika Múdra, Alexandra Kovalčíková, Ľubomír Medvecký: Institute of Materials Research, Slovak Academy of Sciences, Watsonova 47, 040 01 Kosice, Slovakia
Mária Kaňuchová: Technical University of Kosice, Faculty of Mining, Ecology, Process Control and Geotechnology, Letna 9, 042 00 Kosice, Slovakia
Hristo Kolev: Institute of Catalysis, Bulgarian Academy of Sciences, Acad. G. Bonchev St., BU-1113 Sofia, Bulgaria

X-ray photoelectron spectroscopy (XPS) of element core levels is among the most prominent methods applicable for chemical bonding characterization in complex compounds [9-11]. Niobates are characterized by a set of binding energies (BE) related to the maxima of Nb 3d and O 1s lines. The valence state of europium and the Eu 3d core-level XPS spectra of $Eu_mNb_xO_y$ compounds and Eu_2O_3 thin film were studied [12-14]. The splitting of the 3d core level in 3+ and 2+ states interpreted Cho et al. as a consequence of Eu 4f6 and Eu 4f7 final state configurations [15,16]. The ENO compounds seem to be interesting due to the possible existence of the mixed-valence state of Eu ions.

In this work, we prepared $EuNbO_4$ (ENO) precursor by sol-gel method. XPS measurements have been done to investigate the chemical composition and bonding state of ENO phosphor powder. We also report the surface chemistry of ENO thin film prepared by spin-coating and annealed at 1000°C. We have performed a more detailed investigation of the chemical state of the Eu (Eu^{3+} and Eu^{2+}) in ENO.

EXPERIMENTAL

$EuNbO_4$ (ENO) precursor was prepared by the sol-gel method [17] according to Scheme 1. The sol precursor was synthesized from $Eu(NO_3)_3.5H_2O$ and Nb-tartrate complex in solvent ethylene glycol (EG) with a molar ratio of Ln/Nb = 1/1. After homogenization at 80°C, the solution was stirred and heated at 130°C for 5 hours with the formation of transparent viscous sol. The ENO powder precursor was annealed at 1000°C for 1 hour in the air. The Nb-tartrate complex was synthesized by polymer complex method (modified with tartaric acid (TA) instead of citric acid), where $NbCl_5$ was dissolved in ethylene glycol and mixed with chelating agent (tartaric acid) at molar ratio TA:EG = 3:1.

We repeated a similar sol-gel process for the fabrication of thin film. Basic (0.5 M) ENO sol was diluted in stabilization solution (n-propanol). The Al_2O_3 substrate was spin-coated with $PbZrO_3$ (PZ) sol precursor at 2000 rpm for 30 s (PZ interlayer with ~50 nm thickness) followed by drying at 110°C for 3 min and calcining at 400°C for 3 min. The coating cycling was repeated three times to obtain three layers of the thin film. $EuNbO_4$ thin film (~100 nm) was prepared from the ENO sol precursor synthesized in the stoichiometric ratio and deposited on PZ/Al_2O_3 substrate. The final ENO_F film was annealed at 1000°C for 1 hour in the air [17]. The $PbZrO_3$ (PZ) sol was prepared by the sol-gel method [17]. The basic precursors, lead acetate trihydrate and zirconium acetylacetonate were dissolved separately at T = 80°C in acetic acid in two closed flasks. The solutions were dehydrated at 105°C/2 h and after cooling to 80°C they were mixed in the required ratio of Pb:Zr = 1:1. By polycondensation of the formed lead zirconyl acetate precursor, after adding a hydrolyzing agent (ethylene glycol, H_2O, and NH_3(aq)) and the temperature of 80°C, a sol was formed.

The phase compositions of precursor and film were determined by X-ray diffraction analysis (XRD), (a model X' Pert Pro, Philips, The Netherlands) using CuK_α radiation. The surface of ENO powder and film microstructures were characterized using a scanning electron microscope (SEM), (a model JSM-7000F, Jeol, Japan) equipped with an energy dispersive X-ray (EDS) analyzer link ISIS (Oxford, UK).

The surface chemical composition of the samples was analyzed by X-ray photoelectron spectroscopy (XPS). Photoelectron spectroscopy was performed using an XPS instrument (SPECS) equipped with PHOIBOS 100 SCD and a non-monochromatic Al/Mg twin X-ray source. The survey surface spectrum was measured at 70-eV transition energy and high-resolution spectra at 50 eV, at room temperature. All spectra were acquired at a basic pressure of 2×10^{-9} mbar with AlK_α excitation at 10 kV (100 W). The data were analyzed by SpecsLab2 CasaXPS software (Casa Software Ltd). The spectrometer was

calibrated against silver (Ag 3d). All samples showed variable degrees of charging due to their insulating nature. The energy scale has been calibrated by normalizing the C 1s line of adsorbed adventitious hydrocarbons to 285.0 eV. The processing of the measured spectra includes subtraction of X-ray satellites and Shirley-type backgrounds [18]. The peak positions and areas were evaluated by asymmetrical Gaussian-Lorentzian curve fitting. The XPS spectra of Nb, O, and Eu were compared with NIST XPS Database and data published in the literature. The relative concentrations of the different chemical species were determined after normalization of the peak areas to their photoionization cross-sections, calculated by Scofield [19].

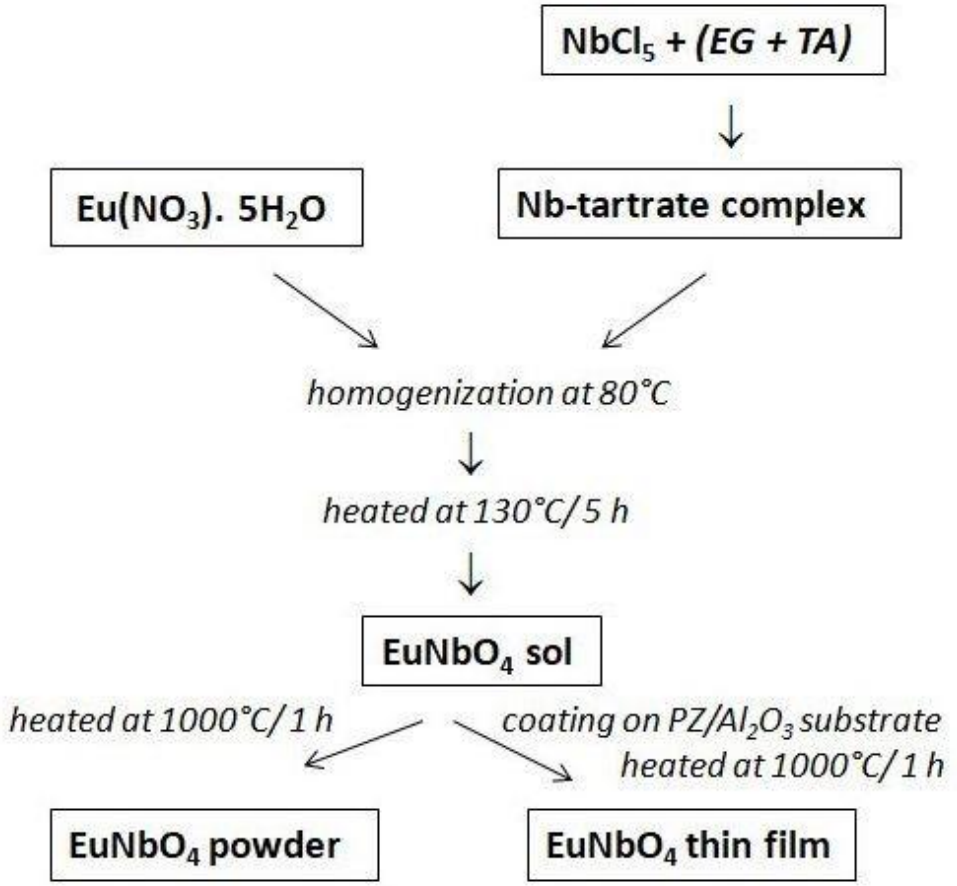

Scheme 1. Preparation route for the ENO powder and ENO_F thin film.

RESULTS AND DISCUSSION

The structures of ENO precursor and ENO_F thin film (after annealing at 1000°C) were studied by the XRD diffractometry and determined different polymorphs (Fig. 1). The XRD patterns verified the formation of monoclinic (M) and tetragonal (T) phases, which

correspond to T-$EuNb_5O_{14}$ (JCPDS 26-0632), M-$EuNbO_4$ (22-1099) in ENO, Fig. 1 shows XRD patterns of the substrate, interlayer, and thin films annealed at 1000°C. XRD analyses verified the formation of the monoclinic ZrO_2 phase (83-0944) and PZ as interlayer on substrate Al_2O_3 and phases: T-$EuNb_5O_{14}$ (main phase) and M-$EuNbO_4$ in ENO_F film.

The particle morphology of the ENO precursor was investigated by SEM (Fig. 2). After annealing at 1000°C, the spherical particle coarsened to the size of about 50-80 nm, and cuboidal 100-150 nm in ENO was observed (Fig. 2(a)). Using the SEM/EDS, local point-by-point probing made it possible to define the position and qualitative composition of such $EuNbO_4$ analyzed in ENO powder at 1000°C. The Eu/Nb atomic ratio was approximately 1.0. In Fig. 2(b), the surface morphology of the film was affected by the introduction of the Eu element resulting in a strong effect on surface roughness ($EuNb_5O_{14}$ particles).

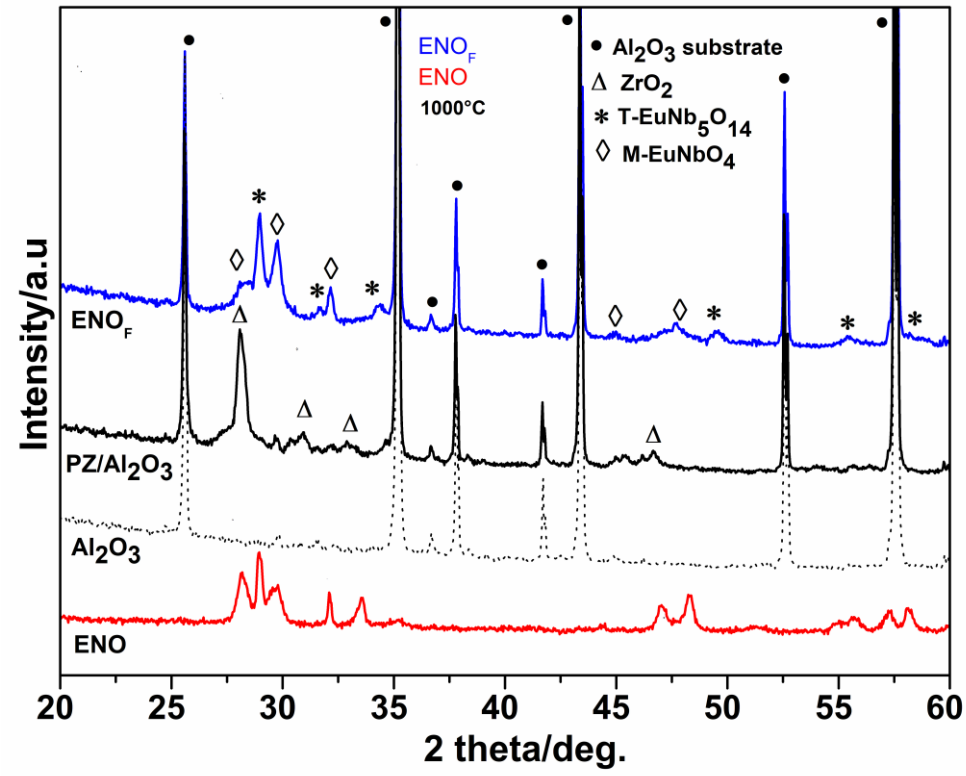

Fig. 1. XRD patterns of $EuNbO_4$ (ENO) precursor and ENO_F thin film on Al_2O_3 substrate with $PbZrO_3$ (PZ) interlayer after annealing at 1000°C.

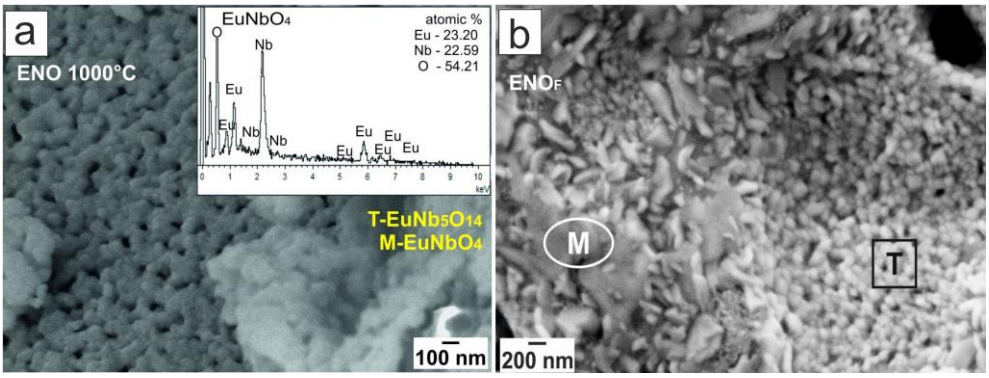

Fig. 2. SEM surface microstructures of (a) ENO precursor and (b) ENO_F thin film.

The XPS was employed to evaluate the surface chemical composition and the oxidation states of individual elements in the powder and thin film. The XPS spectrum of $EuNbO_4$ powder in a wide energy range is shown in Fig. 3(a). Besides carbon, no foreign impurities were found in samples. The survey XPS scans commonly showed Eu 3d, Eu (Auger), Eu 4d, O 1s, C 1s, Nb 3d, and Nb 3p peaks. Fig. 3(a) also presents all peaks related to the ENO: Eu 3d between 1120 ($3d_{5/2}$) and 1190 eV ($3d_{3/2}$) , Nb 3p at 367 ($3p_{3/2}$) and 382 eV ($3p_{1/2}$), Nb 3d at 207 ($3d_{5/2}$) and 209 eV ($3d_{3/2}$). Peaks related to oxygen (O 1s) bonds were observed at around 530 eV and peaks corresponding to O KLL Auger´s line at 973 eV were identified for niobate [20,21]. The XPS survey spectra of ENO_F thin film, substrate Al_2O_3 and PZ interlayer in a wide energy range are shown in Figs. 3(b,c,d). Spectra indicate elements Al, Si from substrates, Pb, Zr, from interlayer, Eu, Nb from the film, C, and O on the film surfaces.

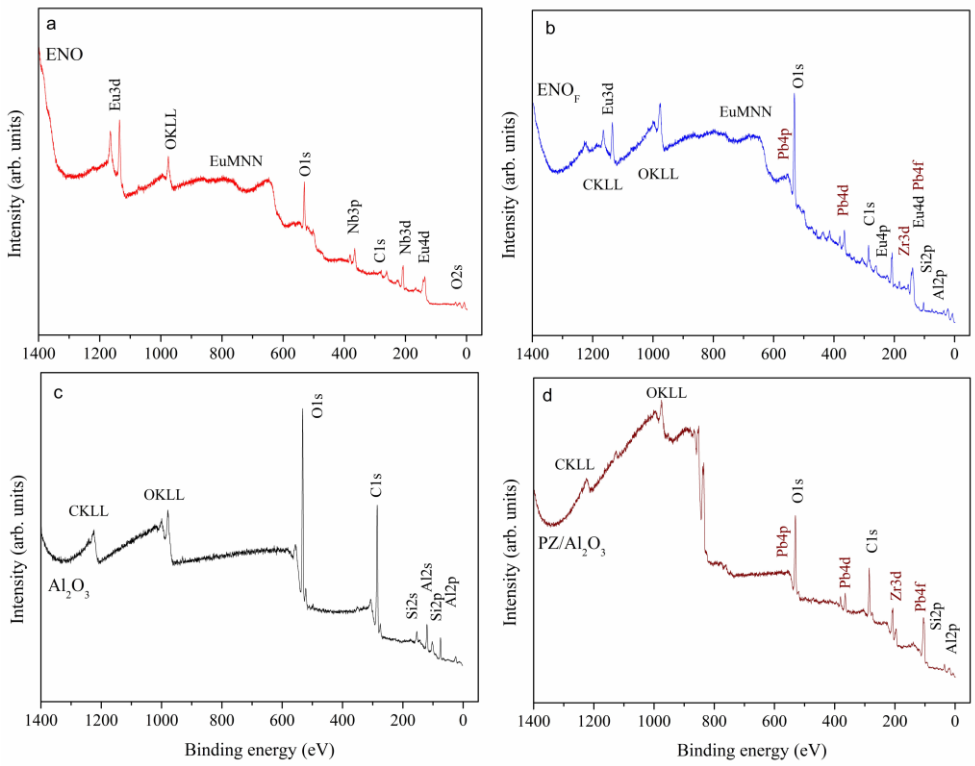

Fig.3. XPS survey spectra of (a) $EuNbO_4$ (ENO) precursor, (b) ENO_F thin film, (c) Al_2O_3 substrate, and PZ interlayer.

The Eu 3d core-level XPS spectra of $EuNbO_4$ powder and thin film and deconvoluted spectra are shown in Figs. 4 and 5. In Fig. 4, the features of Eu $3d_{5/2}$ and Eu $3d_{3/2}$ are fitted with combined Gaussian-Lorentzian functions which reveal 3+ state of Eu (at binding energy 1134.2 eV) with a satellite peak corresponding to 2+ state (1127.1 eV) for Eu $3d_{5/2}$ core level, whereas fitting of Eu $3d_{3/2}$ shows the presence of 3+ state (1164.2 eV) and satellite peak at 1154.5 eV (2+) [12-14]. Cho and Oh [15] labeled prominent peaks as 3+ due to the trivalent $3d^4f^6$ configuration (from bulk) while they labeled other weaker peaks located at a lower BE than the main peak as 2+, which corresponds to the divalent $3d^4f^7$ configuration (from the surface). The contents of Eu^{3+} and Eu^{2+} states were 9 at.% and 1 at.%, respectively in the ENO powder and 2 at.% of Eu^{3+} in the ENO film (Tabs. 1 and 2). The presence of Eu^{2+} states may induce oxygen vacancies in Eu_2O_3 [22].

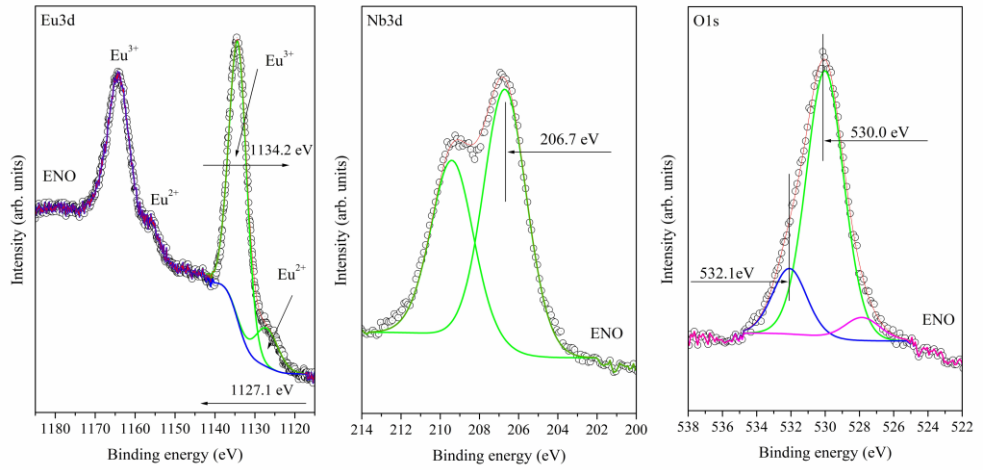

Fig. 4. HR XPS spectra of Eu 3d, Nb 3d, and O 1s and deconvolution peaks for $EuNbO_4$ (ENO) precursor.

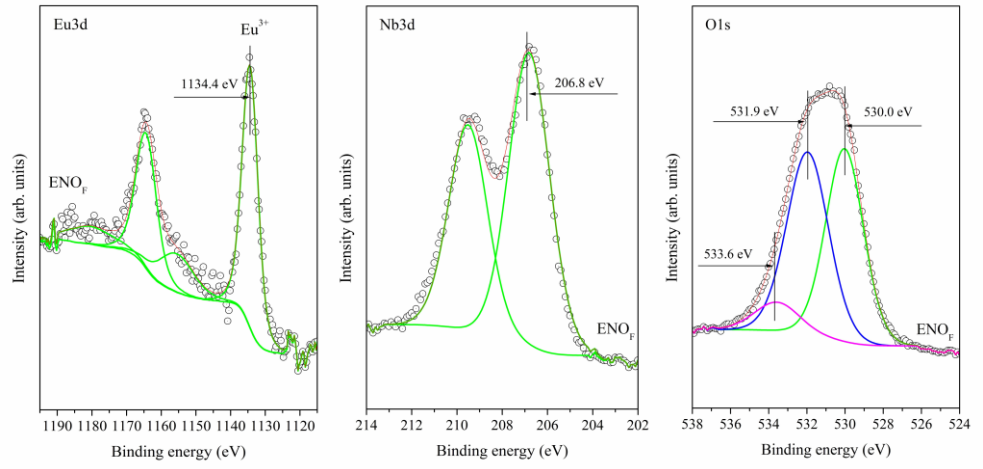

Fig. 5. HR XPS spectra of Eu 3d, Nb 3d, and O 1s and deconvolution peaks for ENO_F thin film.

The High-resolution XPS spectrum of the Eu 3d core level for the ENO_F film is shown in Fig. 5. The doublet at 1134.4 and 1164.2 eV can be attributed to Eu^{3+} $3d_{5/2}$ and $3d_{3/2}$ core levels, respectively. The analysis of peak positions and binding energies in the XPS spectra in the region corresponding to the $3d_{5/2}$ and $3d_{3/2}$ core levels of Eu ion (2 at. %) confirms that Eu characterizes a single Eu^{3+} oxidation state. The peaks of Nb^{5+} 3d centered at 206.7 and 209.5 eV can be assigned to $3d_{5/2}$ and $3d_{3/2}$ states, respectively. The deconvoluted spectrum of O 1s verifies triplet at 527.8, 530.0, and 532.1 eV. The main intense peak centered at 530.0 eV is attributed to the Eu-O and Nb-O in ENO powders [10]. The oxygen ions in the films are bonded to the Eu^{3+} ions. From Tabs. 1 and 2, Eu

concentration (at. %) decreases from 10 % in the precursor to 2 % in the film considering the substrate contains C, Al, Si, Pb, and Zr elements (40 %) at Nb (6 %) and O (52 %).

Tabs. 1 and 2 represent a comparison of Eu, Nb, and O relative concentrations (at.%) in $EuNbO_4$ precursor (Tab. 1) and ENO_F thin film (Tab. 2). The Nd/Nb/O ratio was determined to be 0.7:1.0:4.1 (in precursor) and 0.3:1.0:8.9 (in film). The carbon C 1s is an impurity (C-C and C=O bonds).

Tab. 1. Surface relative concentration (at. %) of $EuNbO_4$ powder after annealing at 1000°C for 1 hour.

Element	**C 1s** (hydrocarbons +CO_3^{2-})		**O 1s**			**Eu 3d** ($3d_{5/2}$, $3d_{3/2}$)		**Nb 3d** ($3d_{5/2}$, $3d_{3/2}$)
Conc. (at. %)	9		66			11		16
Bond	C-H	C=O	Eu MNN	Nb-O Eu-O	non lattice			
Conc. (at. %)	7	2	3.7	51.4	10.9			
Conc. (at. %)	-		73			10		17
			4	57	12	1	9	
BE (eV)	285.0	289.8	527.8	530.0	532.1	1127.1 1157.1 (Eu^{2+})	1134.2 1164.2 (Eu^{3+})	206.7 209.4 (Nb^{5+})
			Eu:Nb:O = 0.7:1.0:4.1			Δ = 30 eV		Δ = 2.7 eV

Tab. 2. Surface relative concentration (at. %) of $EuNbO_4$ film after annealing at 1000°C for 1 hour.

Elem.	**C 1s** (adventitious hydrocarbons)		**O 1s**			**Eu 3d** $3d_{5/2}$ $3d_{3/2}$	**Nb 3d** $3d_{5/2}$ $3d_{3/2}$	**Pb 4f** $4f_{7/2}$ $4f_{5/2}$	**Zr 3d** $3d_{5/2}$ $3d_{3/2}$	**Al 2p**	**Si 2p**
Conc. (at. %)	20		52			2	6	2	2	6	10
Bond	C-H	C-O	Nb-O Eu-O	Eu, Nb-O	OH^-						
Conc. (at. %)	13	7	23	24	5						
BE (eV)	285.0	286.8	530.0	531.9	533.6	1134.4 1164.4 (Eu^{3+})	206.8 209.5 (Nb^{5+})	138.5 143.3 PbO	182.2 184.6 ZrO_2	74.5	102.6
			Eu:Nb:O = 0.3:1.0:8.9			Δ = 30 eV	Δ = 2.7 eV	Δ = 4.87eV	Δ = 2.4eV		

CONCLUSIONS

X-ray photoelectron spectroscopy (XPS) results demonstrate the existence of Eu^{3+} and Eu^{2+} ions in the $EuNbO_4$ precursor. The Eu $3d_{5/2}$ peak consists of strong features characteristic of Eu^{3+} (1134.2 eV) with electron configuration ($4f^5$) and Eu^{2+} (1127.1 eV) with electron configuration ($4f^6$). The molar concentration of Eu^{3+} in ENO was higher (9.0 at.%) than Eu^{2+} (1.0 at.%).

The XPS revealed one valence state of Eu (Eu^{3+}) in the thin film. The relative concentration of Eu on the surface of ENO (10.0 at.%) precursor was higher than thin film (2 at.%). Presently, europium niobates have been observed with XPS, and further accumulation of experimental results is beneficial for the design of new effective electrolytic materials.

ACKNOWLEDGMENT

This work was supported by the Grant Agency of the Slovak Academy of Sciences through project VEGA No. 2/0037/20 and APVV-20-0299.

REFERENCES

[1] Hirano, M., Dozono, H.: Mater. Res. Bull., vol. 50, 2014, p. 213.
[2] Chen, L., Feng J.: Engineering, vol. 6, 2020, p. 178.
[3] Atuchin, VV., Pervukhin, N., Zhang, Z.: Appl. Mechanics Mater., vol. 110, 2012, p. 534.
[4] Voloshyna, O., Boiaryntseva, I., Spassky, D., Sidletskiy, O.: Solid State Phenom., vol. 230, 2015, p. 172.
[5] Graça, MPF., Peixoto, MV., Ferreira, N., Rodrigues, J., Nico, C., Costa, FM., Monteiro, T.: J. Mater. Chem. C., vol. 1, 2013, p. 1.
[6] Liu, L., Chen, Y., Feng, Z., Wu, H., Zhang, X.: Ceram. Int., vol. 47, 2021, p. 4321.
[7] Siqueira, KPF., Lima, PP., Ferreira, RAS., Carlos, LD., Bittar, EM., Matinaga, FM., Paniago, R., Krambrock, K., Moreira, RL., Dias, A.: J. Phys. Chem. C., vol. 119, 2015, p. 17825.
[8] Siqueira, KPF., Moreira. RL., Dias, A.: Chem. Mater., vol. 22, 2010, p. 2668.
[9] Teterin, YA., Bondarenko, TN., Teterin, AY., Lebedev, AM., Utkin, IO.: J. Electron Spectrosc. Relat. Phenom., vol. 88-91, 1998, p. 267.
[10] Teterin, YA., Bondarenko, TN., Teterin, AY., Lebedev, AM., Utkin, IO.: J. Electron Spectrosc. Relat. Phenom., vol. 96, 1998, p. 221.
[11] Thole, BT., van der Laan, G., Fuggle JC., Sawatzky, GA., Karnatak, RC., Esteva, JM.: Phys. Rev. B., vol. 32, 1985, p. 5107.
[12] Mercier, F., Alliot, C., Bion, L., Thromat, N., Toulhoat, P.: J. Electron Spectrosc. Relat. Phenom., vol. 150, 2006, p. 21.
[13] Dilawar, N., Varandani, D., Pandey, VP., Kumar, M., Shivaprasad, SM., Sharma, PK., Bandyopadhyay, AK.: J. Nanosci. Nanotechnol., vol. 6, 2006, p. 105.
[14] Kumar, S., Prakash, R., Choudhary, RJ., Phase, DM.: Mater. Res. Bull., vol. 70, 2015, p. 392.
[15] Cho, EJ., Oh, SJ.: Phys. Rev. B., vol. 59, p. 15613.
[16] Schneider, WD., Laubschat, C., Nowik, I., Kaindl, G.: Phys. Rev. B., vol. 24, 1981, p. 5422.
[17] Brunckova, H., Mudra, E., Medvecky L., Kovalcikova, A., Durisin, J., Sebek, M., Girman, V.: Mater. Des., vol. 134, 2017, p. 455.
[18] Shirley D.: Phys. Rev. B, vol. 5, 1972, p.4709.
[19] Scofield, JH.: J. Electron Spectrosc. Relat. Phenom., vol. 8, 1976, p. 129.

[20] Dutta, A., Saha, S., Kumari, P., Sinha, TP., Shannigrahi, S.: J. Solid State Chem., vol. 229, 2015, p. 296.
[21] Sunding, MF., Hadidi, K., Diplas, S., Løvvik, OM., Norby, TE., Gunnæs, AE.: J. Electron Spectrosc. Relat. Phenom., vol. 184, 2011, p. 399.
[22] Kumar, S., Prakash, R., Choudhary, RJ., Phase, DM.: J. Alloys Compd., vol. 738, 2018, p. 233.

sciendo Powder Metallurgy Progress, Vol.20 (2020), No.2, p.104-110
http://dx.doi.org/10.2478/pmp-2020-0010

ANNOUNCEMENTS

POWDER METALLURGY PROGRESS,

an international open-access journal with 20 years of publishing history announces the

EXTENSION OF THE JOURNAL`S SCOPE

Works from the fields of powder metallurgy, all powder-derived materials - metals, alloys, ceramics, and composites, basic and applied research of materials science related to mechanical and functional properties, manufacturing, and characterization are always welcomed.

But in 2021 the Scope of the Powder Metallurgy Progress will be extended to:

- materials research such as materials physics, materials chemistry, materials engineering, traditional and advanced powder metallurgy, materials processing;
- wide range of metal, ceramic and composite materials including metal matrix, ceramic matrix, polymer matrix composites, and hybrid organic-inorganic-metal-ceramic material systems, structural materials, functional materials, biomaterials, porous materials, magnetic electric and multifunctional materials such as magnetic composites, magnetoelectric, magnetocaloric, ferroelectric, piezoelectric, thermoelectric, magneto-optic, magnetostrictive, or high-temperature materials;
- advanced as well as traditional production technology and processing, additive manufacturing, 3D printing, Press and Sinter, HIP, MIM, PIM, Spark Plasma Sintering, Hot Pressing, Microwave Sintering, Plasma Treatment, Slip Casting, Rapid Heating, Ultrafast Sintering, new progressive compaction and processing methods;
- influence of material processing parameters on their microstructure formation and development and structural relations of physical, mechanical, and functional properties of materials focusing but not limited on powder materials;
- special technological processes of PM material with individual-particular-special physical-chemical properties;
- environmental issues of production and application of PM materials;

- industrial processes, management, and quality, (creation of normative) standard method activity, economical analysis, conception (philosophy) and prediction in PM and progressive material processing field;
- production of technological equipment for powder and advanced materials technology.

For more details visit the PMP homepage.

ANNIVERSARY OF PROF. HERBERT DANNINGER – 65 YEARS

Prof. Dr. Herbert Danninger is an internationally recognized scientific figure in the field of powder metallurgy. He is a co-organizer of several European and world conferences in this field, with many invited lectures. He is the author of more than 520 scientific papers, including monographs and chapters in monographs, peer-reviewed journals, as well as in proceedings of international conferences. His publications have significantly contributed to the development of new technologies, especially in the field of iron powder metallurgy. He is active in the editorial boards of international scientific journals and is an executive editor in the journal Powder Metallurgy. Since 2001, he has been the chairman of the Editorial Board of Powder Metallurgy Progress journal. His help in creating the content and activities of the editorial staff of the PMP magazine from its inception to the present is invaluable. Through his proactive approach, he has helped build a prestigious and competitive international scientific journal.

Professor Danninger has educated dozens of doctoral students who work at various universities around the world and have also found employment in the industrial sphere.

The scientific activity of Prof. Danninger has led to numerous international awards as recognition of his contributions. These include the Skaupy Lecture Award of the Gemeinschaftsausschuss Pulvermetalurgie, Germany, in 2006, the APMI Fellow Award from APMI International, Princeton, NJ, USA, in 2010, and in 2018 he was named a Fellow of the European Powder Metallurgy Association (EPMA). In 2020 he received the Ivor Jenkins Medal, awarded by the UK´s Institute of Materials, Minerals, and Mining.

His scientific and organizational work is also of great importance, as evidenced by the fact that he has been working as the dean of the Faculty of Technical Chemistry, Vienna University of Technology, Vienna, Austria for 8 years. The significant cooperation of Prof. Danninger with companies like Hoganäs, MIBA Austria, and many others have brought a lot of new scientific knowledge and improvements to the industry, which have been applied in practice.

Prof. Danninger, as a colleague, is very accommodating, modest, extremely responsible, and hardworking. We appreciate our cooperation and we wish him good health, lots of new ideas, and success at work on his jubilee.

Profesor Ing. Michal Besterci, DrSc., Dr. h. c.

Dear prof. Danninger, the PMP Editorial Office, members of the Editorial Advisory Board, and also all staff of the IMR SAS, express great thanks for the collaboration and wish many ideas for the scientific and educational activities, good health, and happiness for the future life.

CONFERENCE ANNOUNCEMENT:

15TH LOCAL MECHANICAL PROPERTIES CONFERENCE – LMP2022

Dear colleagues,

The 15th Local Mechanical Properties LMP2022 conference is planned to be held at the Institute of Materials Research of the Slovak Academy of Sciences in Košice, Slovakia, from Wednesday, May 11 to Friday, May 13, 2022., as a continuation of the successful meetings LMP from previous years (Košice 2004 and 2005, Plzeň – Nečtiny 2006, Brno – Šlapanice 2007, Herľany 2008, Telč 2009, Smolenice 2010, Olomouc 2011, Levoča 2012, Kutná Hora 2013, Stará Lesná 2014, Liberec 2015, Košice 2017 and Prague 2019).

The scope of the conference is traditionally focused on the results of research and development in the field of materials engineering, experimental methods, modeling, etc., with the aim to characterize the mechanical properties of materials from nano to micro/mesoscale. Contributions on indentation and other methods of hardness and other mechanical properties assessment, measurement of deformations and stresses, time-dependent properties with related microstructure analyses (TEM/SEM, FIB, AFM, etc.) regardless of material type (metals, ceramics, plastics, biomaterials, concrete, etc.) are welcome.

The conference will be held at the premises of the Institute of Materials Research of the Slovak Academy of Sciences in Košice. The possibilities for accommodation in Košice are indicated on the conference website.

The conference language will be English. The conference will include invited lectures, oral and poster presentations. During the conference, the participation of Ph.D. students in the LMP Poster Award competition is encouraged. The accepted contributions will be reviewed and

published in the Special Issue of the journal "Powder Metallurgy Progress" which is an Open Access journal indexed by the Scopus database.

The early bird (prior to April 30, 2022) conference fee is 350 €, the regular fee is 380 €. For Ph.D. students, a reduced (early bird) fee of 250 € and 300 € (regular, after the deadline) are offered. The conference fee covers the organization of the conference, refreshment, and catering during the conference, gala-diner and social program, and the expenses for the publication of the accepted papers in a special issue of PMP journal.

Sponsors of the conference and exhibitors are welcomed.

Hopefully, the limitations on traveling and social contacts will be over by next November and LMP 2022 will provide again a possibility to re-establish the old to create new scientific and personal contacts, to gain and exchange knowledge and experience in a friendly atmosphere. Stay healthy and see you at LMP 2022 in Kosice.

František Lofaj
Chair of the conference

IMPORTANT DATES:

April 15, 2022	Abstract submission and registration
April 30, 2022	Notification of acceptance
April 30, 2022	Early bird conference fee payment
May 5, 2022	Final program
May 11-13, 2022	Manuscript submission and conference